Supporting Information:

Spectator-metal ion guided redox-dominant cobalt oxy hydroxide as a high-performance supercapacitor

Experimental Section:

Cobalt nitrate hexahydrate (Co $(NO_3)_2.6H_2O$), Urea (CH_4N_2O), Nickel Chloride hexahydrate ($NiCl_2.H_2O$), Manganese chloride tetrahydrate ($MnCl_2.4H_2O$) Ammonium metavanadate (NH_4VO_3) are from Sigma Aldrich and Carbon paper (CP) was from Alfa Aesar. KOH was from Merck. All the chemicals used as received without further purification.

Synthesis Of CoVO (OH):

Cobalt and vanadium precursors are taken in different ratios (1:0,2:1,1:1,1:2) dissolved in 25mL deionized water followed by the addition of NH_4Cl(2.5mmol) and CH_4N_2O (4mmol) and hydrothermally treated at 120^0C in a 50mL Teflon autoclave with activated CP [1] for 8h. The synthesized product grown on CP is cleaned with deionized water and absolute ethanol and dried overnight in vacuum oven. The electrodes were named according to their molar ratio of cobalt and vanadium. (COV11 indicates Co:V = 1:1)

Synthesis Of NiMn-LDH@CoVO (OH):

To prepare NiMn-LDH@CVO, $NiCl_2.6H_2O$, $MnCl_2.4H_2O$ in 3:1 ratio and hexamine(2mmol) dissolved in 35mL deionized water, hydrothermally treated along with CoVO(OH)/CP substrate at 90^oC for 8h. [2]

Materials Characterization

GAMRY Instruments (Interface 1010E) tested the electrochemical properties of synthesized samples. Powder X-ray diffraction (PXRD) was performed using Rigaku SmartLab X-ray diffractometer with a Cu K_α (λ = 1.54 Å) source with a 9kW rotating anode.

A field-emission scanning electron microscope (Sigma 300) at 5 kV and a transmission electron microscope (JEOL JEM-2100F) with an operating voltage of 200 kV were used to investigate the morphology and microstructure of the catalyst, respectively. Electron-dispersive X-ray (EDX) spectroscopy (Sigma 300, Zeiss) was used for surface elemental analysis.

Electrochemical measurements:

Before the electrochemical measurements, mass loading of the catalyst was calculated by taking mass difference before and after hydrothermal deposition and mass loading was found to be 0.3mg per 0.5x1cm^2 area. The electrochemical properties of synthesized samples were tested by GAMRY Instruments (Interface 1010E). The as prepared catalyst on carbon paper was used as the working electrode, Pt wire as counter electrode, and a Hg/HgO as reference electrode in 1 M KOH liquid electrolyte at room temperature. Cyclic Voltammetry (CV) tests were performed at -0.1-0.6V voltage at 10-100mV s^{-1} scan rates and the charge discharge tests were performed at same voltage ,1-10 Ag^{-1} current density. The Electron Impedance spectroscopy (EIS) tests were performed at the open circuit potential frequency range of 0.1-10^{5}Hz. The specific capacitance (*Cs*) of electrodes was calculated from galvanostatic discharge curves using following equation:

$$Cs = \frac{I * \Delta t}{\Delta V * m} \quad \ldots\ldots\ldots\ldots\ldots\ldots (1)$$

Where C_s is the specific capacitance (Fg^{-1}), I is applied current(A), Δt is the discharge duration(sec), ΔV is the potential window(V).

Two Electrode System:

The ASCs were assembled with two pieces of carbon paper sheet electrodes with the active material added as the positive electrode, activated carbon as negative electrode and 1M KOH as the electrolyte. The energy density E (Wh kg^{-1}) and power density P (W kg^{-1}) of the electrodes were calculated by following equations:

$$E = \frac{1}{2 * 3.6} Cs\Delta V2 \quad \text{..... (2)}$$

$$P = \frac{E \times 3600}{\Delta t} \quad \text{..... (3)}$$

The preparation steps of all-solid ASCs are as follows: A slurry consisting of AC , 5μL of nafion and *N*-methyl-2-pyrrolidone (NMP) solution was prepared. The slurry concentration was adjusted by adding NMP to prevent agglomeration. After the preparation of slurry, it was coated on CP. The quantity of AC is determined by the following formula

$$\frac{m^+}{m^-} = \frac{C^+ \Delta V^+}{C^- \Delta V^-} \quad \text{..... (4)}$$

where m, C, and ΔV represent the active load of the electrodes, specific capacitance, and voltage window.

Then 1 g of PVA and 15 mL of deionized water were added to a beaker and heated to 85 °C for 1 h, and the PVA was completely dissolved into a gel. When the temperature was naturally cooled to 60 °C, 15 mL of 1 M KOH was added to the PVA gel, stirred evenly, and allowed to stand until cooled to room temperature to obtain a PVA-KOH gel. The PVA-KOH gel was evenly coated on the positive and negative electrodes, and then, the positive and negative electrodes were glued together up and down without contact between the positive and negative electrodes, and the gel surface solidified by standing in the air. In this way, the NiMn-LDH@COV/CP//AC/CP all-solid-state ASC device was assembled.

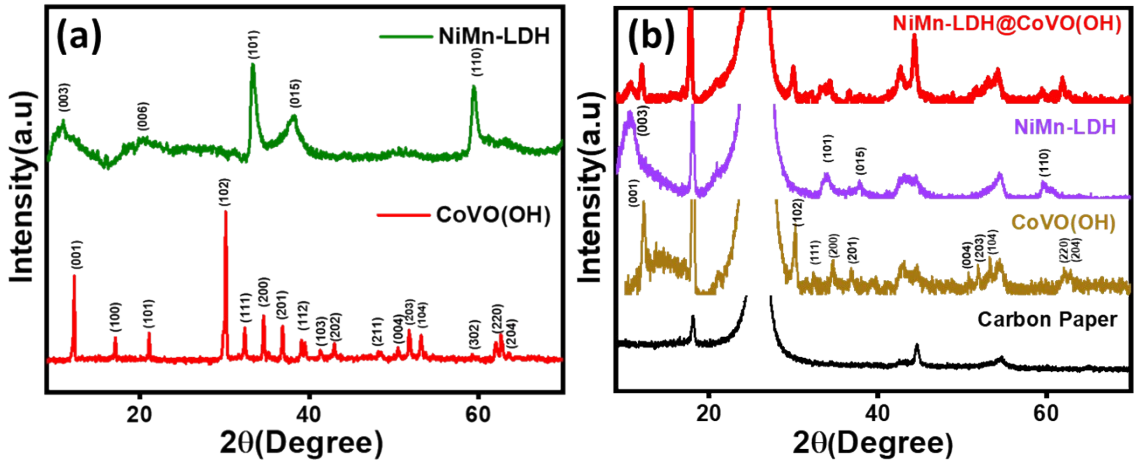

Figure S1: (a) Powder X-ray diffraction (b)Thin film XRD of CoVO(OH), NiMn-LDH and NiMn-LDH@CoVO(OH) on carbon paper

The formation and phase purity of the as-synthesized materials were confirmed using powder X-ray diffraction (PXRD) method. Fig. S1(a) shows the XRD pattern of bare COV (CoVO(OH)) and NiMn-LDH. All the peaks are indexed with no impurity peaks. The COV corresponds to the hexagonal phase (JCPDS no. 00-057-0519) while the NiMn-LDH corresponds to the rhombohedral phase (JCPDS no. 38-0715). The peak at ~10° (2θ) for the NiMn-LDH corresponds to the interlayer spacing of LDH sheets in the "*c*" direction (003 plane) with interplanar spacing of ~1.19 nm, confirming its two-dimensional (2D) nature. The XRD spectra of the fabricated electrodes, COV/CP and NiMn-LDH@COV/CP, are demonstrated in Fig. S1(b).

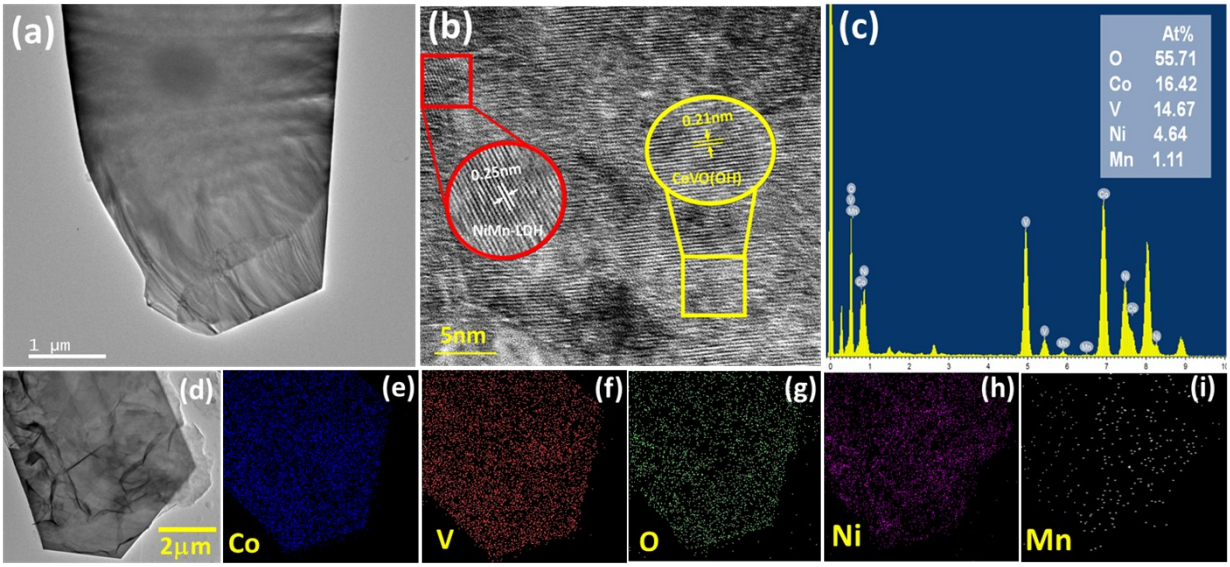

Figure S2: FETEM image of (a) bare COV hexagonal plates (b)HRTEM image of the composite with *d*-spacing values corresponding to respective planes of individual materials, (c) EDX spectra of NiMn-LDH@COV (d) FETEM image of NiMn-LDH@COV showing the presence of nanosheets over the hexagonal sheet structure (e-i) EDS mapping of composite showing the presence of (e) cobalt, (f) vanadium, (g) oxygen, (h) nickel and (i) manganese.

The sheet structures of the as-synthesized materials were further confirmed using field emission transmission electron microscopy (FETEM) technique. The high-resolution transmission electron microscope (HRTEM) image of the composite was recorded to further validate the presence of NiMn-LDH over the COV surface. Fig. S(2b) shows the HRTEM image with two different lattice fringes. The *d*-spacing value of 0.21nm corresponds to the (202) plane of CoVO(OH) and 0.25nm corresponds to (015) plane of NiMn-LDH. The scanning transmission electron microscopy energy-dispersive X-ray spectroscopy (STEM-EDX) elemental mapping was recorded for the composite to show the presence of all the elements (Fig. S2e-g) cobalt, vanadium, and oxygen in the hexagonal sheet structure and Fig. S2(h,i) shows the presence of nickel and manganese confirming the homogenous deposition of the LDH over the COV.

X-Ray Photoelectron Spectroscopy:

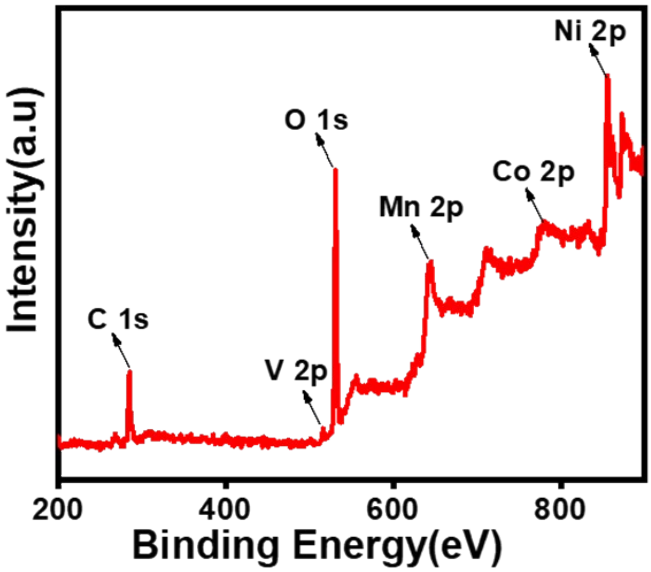

Figure S3: XPS survey spectra of NiMn-LDH@COV showing the presence of all the constituent elements

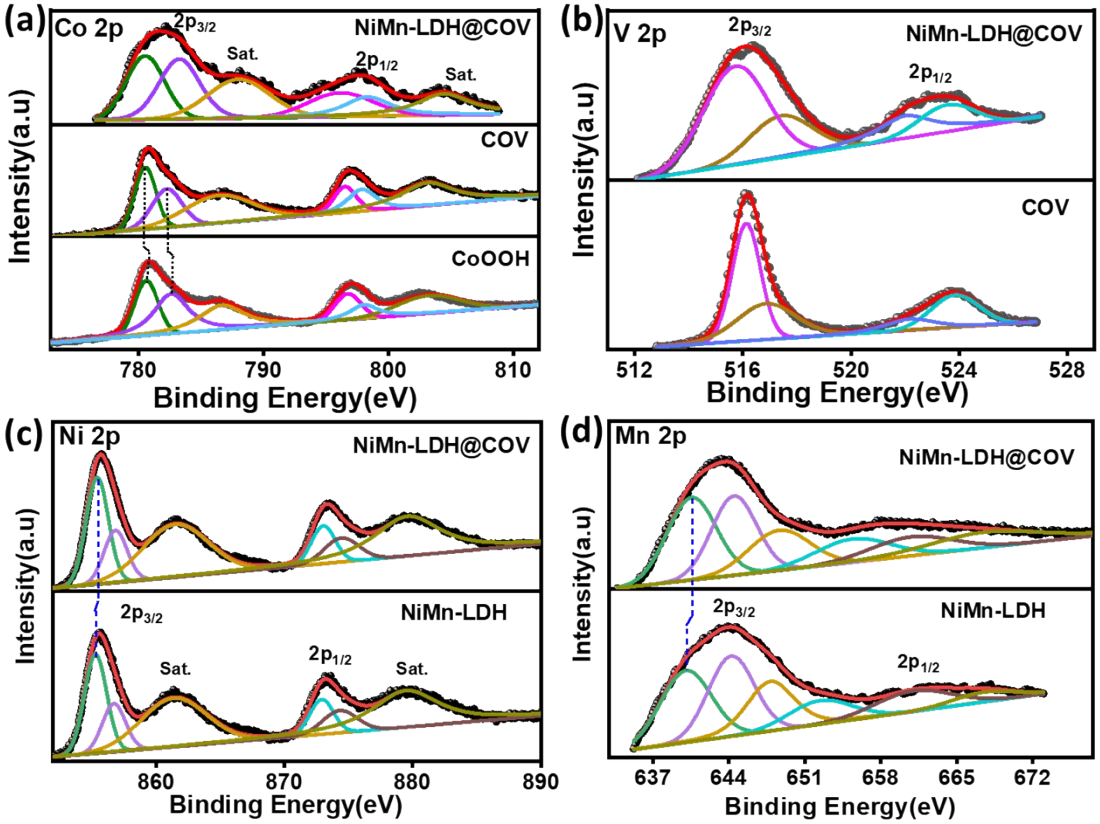

Figure S4: (a) Co 2p of CoOOH, COV and NiMn-LDH@COV (b) V 2p of COV and NiMn-LDH@COV and (c,d) Ni 2p and Mn 2p of NiMn-LDH and NiMn-LDH@COV, respectively.

To investigate the electronic and valence state of elements present in the synthesized material X-ray Photoelectron spectroscopy was utilized. Fig S3(a) shows Co 2p core level spectra CoO(OH), COV, and NiMn-LDH@COV. In CoO(OH), the $2p_{3/2}$ peak at 780.61 eV and $2p_{1/2}$ peak at 782.46 eV confirms the presence of Co^{3+}, while the $2p_{3/2}$ peak at 796.60and $2p_{1/2}$ peak at 798.02eV confirms the presence of Co^{2+}. Co $2p_{3/2}$ and Co $2p_{1/2}$ are energetically separated by about 15.9 eV. The shake-up satellite peaks are observed at 786.52 and 803.13 for Co $2p_{3/2}$ and $2p_{1/2}$, respectively. After the incorporation of vanadium(V^{5+}) into CoO(OH), the valence state of Co shifted from Co^{2+} to Co^{3+} and red-shifted by ~0.23 eV showing strong electronic interaction between Cobalt and vanadium. V^{5+} has a vacant orbital, where there is partial charge transfer from Cobalt to Vanadium there by increasing the faradic reaction. Again, in the composite NiMn-LDH@COV, Co2p core level spectra exist with a blue shift in binding energy. From the core-level V 2p spectra Fig. S2(b) of COV and NiMn-LDH@COV it is confirmed that Vanadium is present in both +4 and +5 oxidation states. Fig S2(c,d) showing Ni and Mn core level 2p spectra, where Ni is in +2 and +3 oxidation states and Mn is in +3 and +4 oxidation states in the composite NiMn-LDH@COV and NiMn-LDH. There is a shift in the peak position of Ni 2p and Mn 2p core-level spectra toward higher binding energy, which indicates good electronic interaction between NiMn-LDH nanosheets and COV hexagonal plates in the composite material.

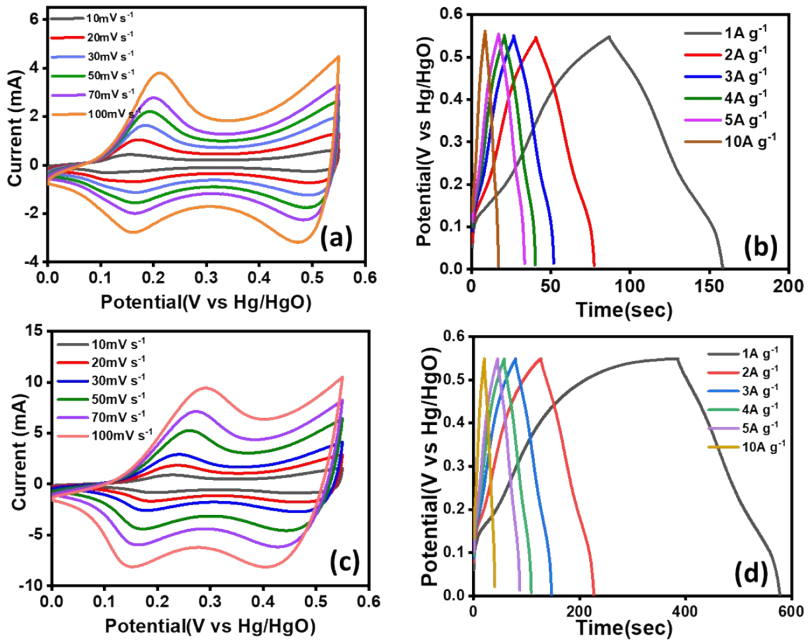

Figure S5: (a, c) CV plots and (b, d) representing GCD plot of the CoO(OH), COV/CP, measured at different scan rates (10-100mV s^{-1}) and different current densities(1Ag^{-1} to 10Ag^{-1}) with different cobalt and vanadium ratio i.e COV(1:0), COV(1:1), respectively

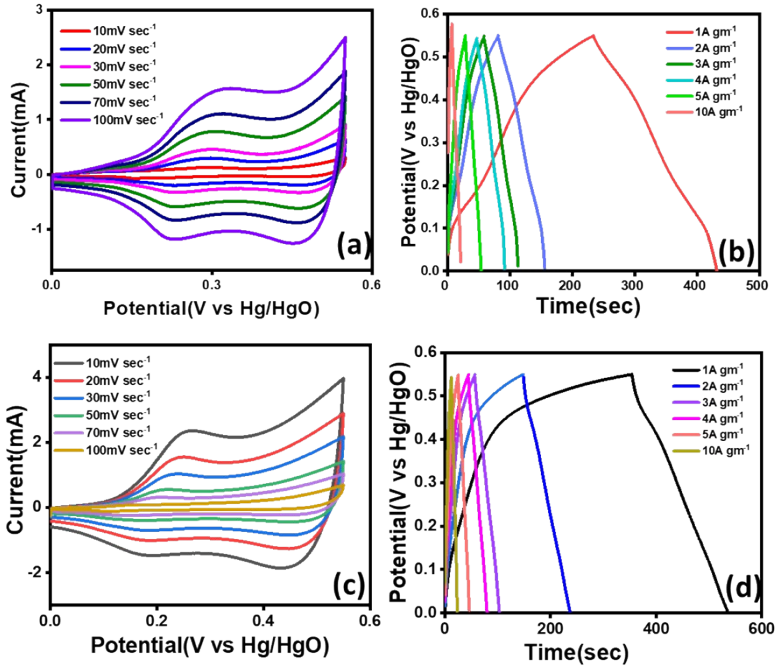

Figure S6: (a,c) CV plots and (b,d) representing GCD plot of the COV/CP, measured at different scan rates (10-100mVs^{-1}) and different current densities(1Ag^{-1} to 10Ag^{-1}) with different cobalt and vanadium ratio i.e COV(2:1),COV(1:2), respectively.

The choice of the best-performing bare electrode (**COV**) was also confirmed by obtaining the GCD curves for all the different **COV** materials (with different Co and V ratios) (Fig. S5 and Fig. S6). The C_s values at 1 Ag^{-1} was calculated using equation (eq. S1) were found to be 181 Fg^{-1} ,425 Fg^{-1}, 345 Fg^{-1} and 505 Fg^{-1} for **COV** (1:0), **COV** (2:1), **COV** (1:2) & **COV** (1:1), respectively.

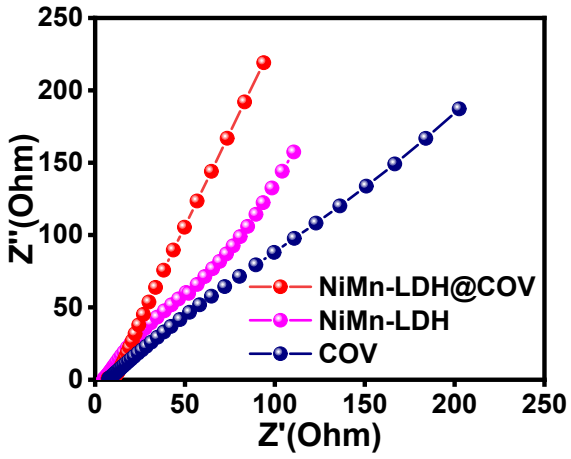

Figure S7: Nyquist plot of all the electrodes obtained from EIS measurement

Fig. S7 shows the Nyquist plot of the bare and composite electrodes obtained by the EIS technique. The R_{ct} values were then evaluated by fitting the Nyquist plots to a suitable electrical circuit. The lower R_{ct} value for the composite, NiMn-LDH@**COV**, (26 Ω) compared to that of bare **COV** (43 Ω) and NiMn-LDH (50 Ω) proves the facile charge transfer process occurring at the electrolyte interface during the cyclic redox reactions. The low resistance can also be attributed to the enlarged specific surface area of the composite electrode material and strong interaction between the nanosheet structures (NiMn-LDH) and hexagonal sheets (**COV**) accelerating the ion transfer processes. Additionally, the steeper slope at low-frequency region for the composite confirms its higher capacitive nature due to the lower diffusive resistance of the electrolyte ions.

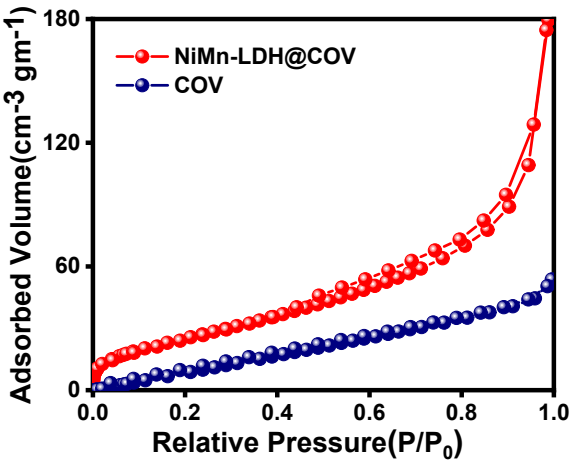

Figure S8: (a)N_2 adsorption and desorption curves of bare and composites

From the adsorption-desorption curve, the surface area of COV and NiMn-LDH@COV was found to be 42 m^2 gm^{-1} and 120.43 m^2 gm^{-1} respectively.

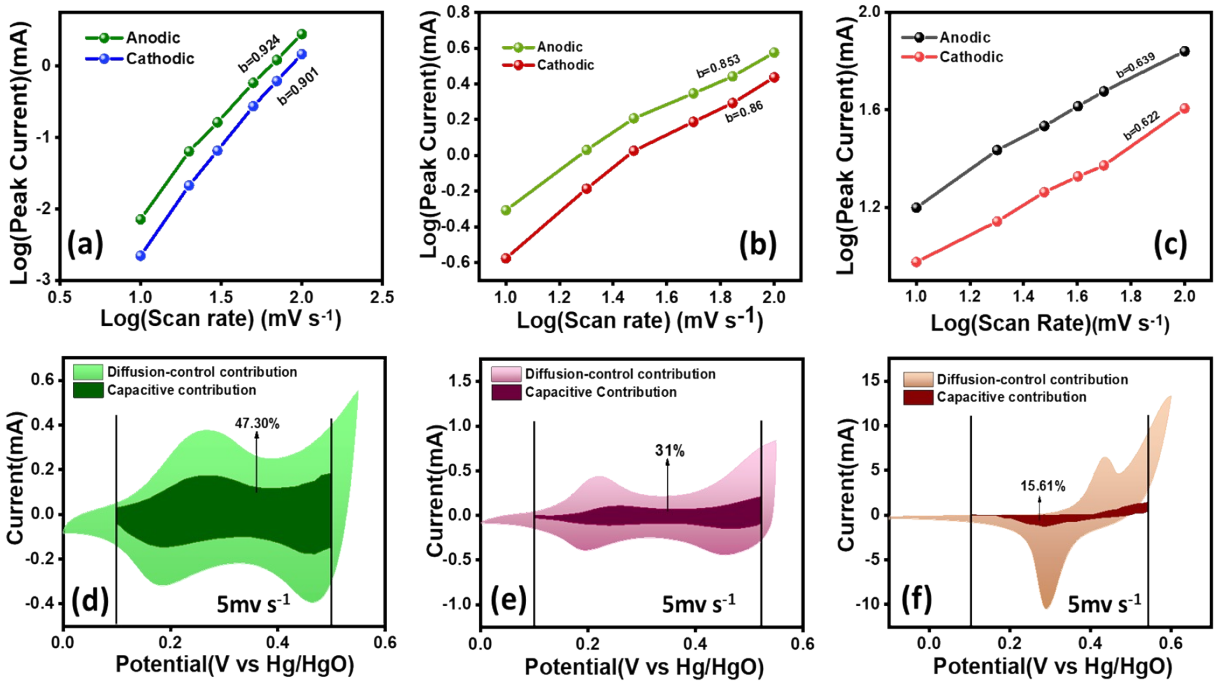

Figure S9: The plot of log(*i*) *versus* log(*v*) of (a) CoOOH (b)bare COV (c) NiMn-LDH@CoVO(OH) comparison of capacitive and diffusive controlled contribution in cyclic voltammetry curve at scan rate of 5 mVs^{-1} for (d)CoOOH (e) COV (f) NiMn-LDH@COV,respectively.

The charge storage mechanism storage of the samples was analysed by electrochemical measurement combined with the formulas,

$$i = av^b \quad \text{..... (5)}$$

$$i = k_1 v + k_2 v^{1/2} \quad \text{..... (6)}$$

Where a and b are constants, v (mV s^{-1}) represents the scan rate i (A) is the peak current at v ·The value of b = 0.5 represents a diffusion-controlled process, whereas value of b =1 indicates a surface-controlled process. For the NiMn-LDH@COV, the b-values of the cathodic and anodic peaks are calculated to be 0.622 and 0.639, respectively, capacitance-controlled pseudocapacitance-type behaviour and diffusion-controlled battery-type behaviour.[9,10] Fig S7(d,e,f) displays the CV curves of diffusion-controlled contribution and capacitive contribution of CoOOH,COV and NiMn-LDH@COV electrodes, respectively at a low scan rate of 5 mV s^{-1}. From the fig. S7(f), composite NiMn-LDH@COV electrode material is storing energy by a diffusive controlled process. Also, at low scan rate, the composite electrode acquires sufficient time to diffuse into the electrode surface and complete the faradaic redox reaction, resulting in a higher diffusion percentage from overall capacity showing a battery-type behaviour.

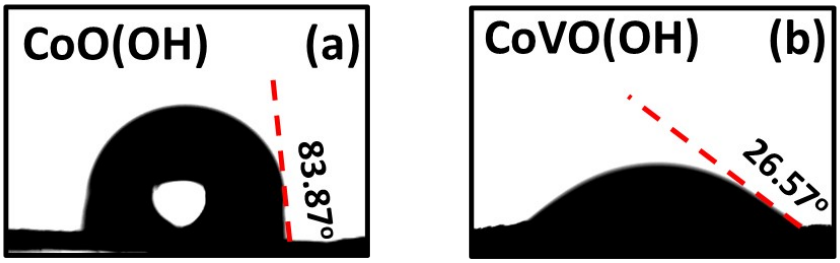

Figure S10: Contact-angle measurements of (a)CoO(OH) (b)CoVO(OH)

From the Contact angle analysis, it is seen that, the surface of CoVO(OH) electrode showed a contact angle of 26.57° which is smaller than CoO(OH) (83.57°) suggesting the enhancement of surface hydrophilicity due to the presence of V^{5+}.

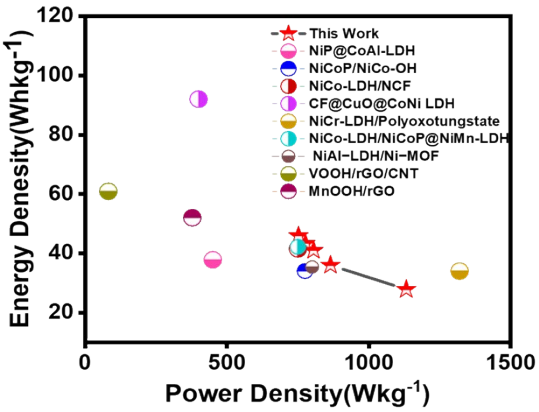

Figure S11: Ragone plot of the ASC device.

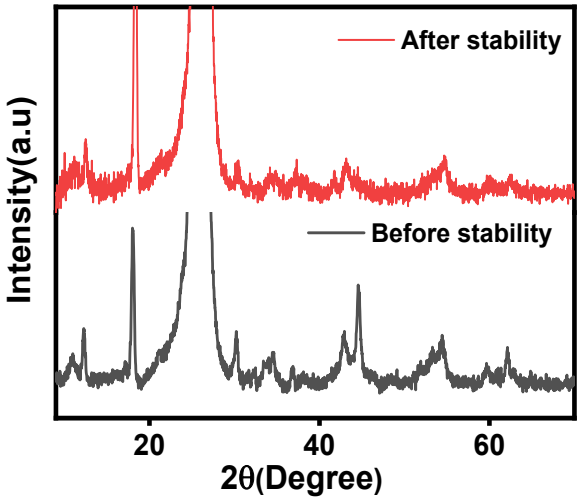

Figure S12: Thin film XRD of NiMn-LDH@CoVO(OH) before and after stability test

Figure S12 shows the XRD NiMn-LDH@CoVO(OH) before and after the stability test, where no changes in the structural composition are seen, which further substantiates the stability of the prepared catalyst.

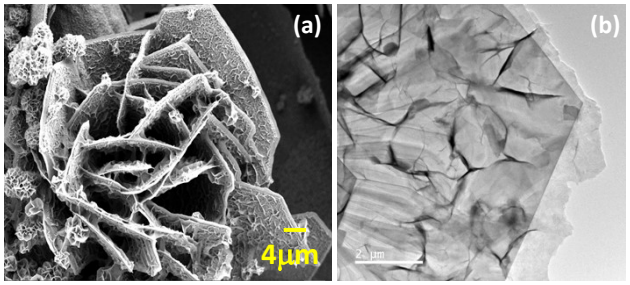

Figure S13: FFESEM and FETEM image of NiMn-LDH@CoVO(OH) after stability test

Figure S13 shows the FESEM and FETEM image of NiMn-LDH@CoVO(OH) after the stability test, which shows that the hexagonal morphology with nanosheets is retained after the 5000 charge-discharge cyclic stability test.

Electrode material	Specific capacitance	Electrolyte	References
NiMn LDH@CoVO(OH)/CP	**1700 F g^{-1} at 1A g^{-1}**	**1M KOH**	**This Work**
VOx(OH)y/CNT/rGO	414 F g^{-1}at 0.5 A g^{-1}	1mol L^{-1} $LiClO_4$/propylene carbonate	3
MnOOH/3D-rGO	327 Fg^{-1}at 0.2A g^{-1}	1M Na_2SO_4	4
NiCoOOH/NF	34.8 mAh cm^{-2} 5 mA cm^{-2}	1M KOH	5
NiOOH@FeOOH Nanosheet	748.13 mF cm^{-2} at 1.5 mA cm^{-2}	1M KOH	6
$VO(OH)_2$ nanorods	198 F·g^{-1} 0.5 A g^{-1}	1 mol L^{-1} Na_2SO_4	7
NiCoLDH@NiOOH	2622 F g^{-1} at1 A g^{-1}	6.0 M KOH	8
NiP/CoAl-LDH	556 C g^{-1} at1mA cm^{-2}	2 M KOH	11
NiCoP/NiCo-LDH	1100 F g^{-1} at1 A g^{-1}	3 M KOH	12
NiCo-LDH/N-doped carbon foam	1512 F g^{-1} at 0.5 A g^{-1}	2 M KOH	13
CF@CuO@CoNi-LDH	797.85 F g^{-1} at1 A g^{-1}	2 M KOH	14
NiCr-LDH/Polyoxotungstate	736 Cg^{-1} at 1 A g^{-1}	2 M KOH	15
NiCo-LDH/NiCoP@NiMn-LDH	2318 F g^{-1} at 1 A g^{-1}	6 M KOH	16

Table S1: Comparison of the performances reported in our work with those recently reported on transition metal oxyhydroxide-related materials for supercapacitors.

References:

1. C. T. Moi, S. Bhowmick and M. Qureshi, *ACS Appl. Mater. Interfaces*, 2021, 13, 51151–51160
2. H. Liang, J. Lin, H. Jia, S. Chen, J. Qi, J. Cao, T. Lin, W. Fei and J. Feng, *J. Mater. Chem. A*, 2018, 6, 15040–15046.
3. M. Chen, Y. Zhang, Y. Liu, Q. Wang, J. Zheng and C. Meng, *ACS Appl. Energy Mater.,* 2018, 5527−5538.
4. S. Sun, S. Wang, T. Xia, X. Li, Q. Jin, Q. Wu, L. Wang, Z. Wei and P. Wang, *J. Mater. Chem. A*, 2015, 3, 20944–20951.
5. M. Gao, Y. Li, J. Yang, Y. Liu, Y. Liu, X. Zhang, S. Wu and K. Cai, *Chem. Eng. J*, 2022, 429, 132423.
6. D. Zhang, X. Kong, M. Jiang, D. Lei and X. Lei, *ACS Sustain Chem. Eng.*, 2019, 7, 4420–4428.
7. M. Chen, Y. Zhang, J. Zheng, Y. Liu, Z. Gao, Z. Yu and C. Meng, *Mater. Lett.*, 2018, 227, 217–220.
8. H. Liang, J. Lin, H. Jia, S. Chen, J. Qi, J. Cao, T. Lin, W. Fei and J. Feng, *J Power Sources*, 2018, 378, 248–254.
9. Z. Yuan, H. Wang, J. Shen, P. Ye, J. Ning, Y. Zhong and Y. Hu, *J. Mater. Chem. A*, 2020, **8**, 22163–22174.
10. H. Fu, A. Zhang, F. Jin, H. Guo and J. Liu, *ACS Appl. Mater. Interfaces*, 2022, **14**, 16165–16177
11. S. Wang, Z. Huang, R. Li, X. Zheng, F. Lu and T. He, *Electrochim. Acta*, 2016, 204, 160–168.
12. X. Li, H. Wu, A. M. Elshahawy, L. Wang, S. J. Pennycook, C. Guan and J. Wang, *Adv Funct. Mater.,* 2018, 28, 1800036.
13. Y. Liu, Y. Wang, C. Shi, Y. Chen, D. Li, Z. He, C. Wang, L. Guo and J. Ma, *Carbon*, 2020, 165, 129–138.
14. F. Chen, C. Chen, Q. Hu, B. Xiang, T. Song, X. Zou, W. Li, B. Xiong and M. Deng, *Chem. Eng. J.*, 2020, 401, 126145.

15. N. S. Padalkar, S. v. Sadavar, R. B. Shinde, A. S. Patil, U. M. Patil, D. S. Dhawale, R. N. Bulakhe, H. Kim, H. Im, A. Vinu, C. D. Lokhande and J. L. Gunjakar, *J. Colloid Interface Sci.*, 2022, 616, 548–559.
16. H. Liang, J. Lin, H. Jia, S. Chen, J. Qi, J. Cao, T. Lin, W. Fei and J. Feng, *J. Mater. Chem. A*, 2018, 6, 15040–15046.
17. W. Zheng, S. Sun, Y. Xu, R. Yu, and H. Li, *ChemElectroChem*, 2019, 6, 3375–3382.